

**This is a self-archived version of an original article. This version may differ from the original in pagination and typographic details.**

**Author(s):** Gell, Lars; Lempelto, Aku; Kiljunen, Toni; Honkala, Karoliina

**Title:** Influence of a Cu–zirconia interface structure on CO<sub>2</sub> adsorption and activation

**Year:** 2021

**Version:** Published version

**Copyright:** © 2021 Author(s).

**Rights:** In Copyright

**Rights url:** <http://rightsstatements.org/page/InC/1.0/?language=en>

**Please cite the original version:**

Gell, L., Lempelto, A., Kiljunen, T., & Honkala, K. (2021). Influence of a Cu–zirconia interface structure on CO<sub>2</sub> adsorption and activation. *Journal of Chemical Physics*, 154(21), Article 214707. <https://doi.org/10.1063/5.0049293>

# Influence of a Cu–zirconia interface structure on CO<sub>2</sub> adsorption and activation

Cite as: J. Chem. Phys. **154**, 214707 (2021); <https://doi.org/10.1063/5.0049293>

Submitted: 03 March 2021 • Accepted: 17 May 2021 • Published Online: 03 June 2021

 Lars Gell,  Aku Lempelto,  Toni Kiljunen, et al.



View Online



Export Citation



CrossMark

## ARTICLES YOU MAY BE INTERESTED IN

[A consistent and accurate ab initio parametrization of density functional dispersion correction \(DFT-D\) for the 94 elements H-Pu](#)

The Journal of Chemical Physics **132**, 154104 (2010); <https://doi.org/10.1063/1.3382344>

[Grand-canonical approach to density functional theory of electrocatalytic systems: Thermodynamics of solid-liquid interfaces at constant ion and electrode potentials](#)

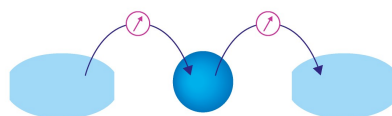
The Journal of Chemical Physics **150**, 041706 (2019); <https://doi.org/10.1063/1.5047829>

[Escaping scaling relationships for water dissociation at interfacial sites of zirconia-supported Rh and Pt clusters](#)

The Journal of Chemical Physics **151**, 164302 (2019); <https://doi.org/10.1063/1.5126261>

Webinar

Interfaces: how they make  
or break a nanodevice



March 29th – Register now



# Influence of a Cu-zirconia interface structure on CO<sub>2</sub> adsorption and activation

Cite as: J. Chem. Phys. 154, 214707 (2021); doi: 10.1063/5.0049293

Submitted: 3 March 2021 • Accepted: 17 May 2021 •

Published Online: 3 June 2021



View Online



Export Citation



CrossMark

Lars Gell,  Aku Lempelto,  Toni Kiljunen,  and Karoliina Honkala<sup>a)</sup> 

## AFFILIATIONS

Department of Chemistry, Nanoscience Center, University of Jyväskylä, P.O. Box 35 (YN), Jyväskylä FI-40014, Finland

<sup>a)</sup> Author to whom correspondence should be addressed: [karoliina.honkala@jyu.fi](mailto:karoliina.honkala@jyu.fi)

## ABSTRACT

CO<sub>2</sub> adsorption and activation on a catalyst are key elementary steps for CO<sub>2</sub> conversion to various valuable products. In the present computational study, we screened different Cu–ZrO<sub>2</sub> interface structures and analyzed the influence of the interface structure on CO<sub>2</sub> binding strength using density functional theory calculations. Our results demonstrate that a Cu nanorod favors one position on both tetragonal and monoclinic ZrO<sub>2</sub> surfaces, where the bottom Cu atoms are placed close to the lattice oxygens. In agreement with previous calculations, we find that CO<sub>2</sub> prefers a bent bidentate configuration at the Cu–ZrO<sub>2</sub> interface and the molecule is clearly activated being negatively charged. Straining of the Cu nanorod influences CO<sub>2</sub> adsorption energy but does not change the preferred nanorod position on zirconia. Altogether, our results highlight that CO<sub>2</sub> adsorption and activation depend sensitively on the chemical composition and atomic structure of the interface used in the calculations. This structure sensitivity may potentially impact further catalytic steps and the overall computed reactivity profile.

Published under an exclusive license by AIP Publishing. <https://doi.org/10.1063/5.0049293>

## I. INTRODUCTION

Chemical transformations of CO<sub>2</sub> into fuels and platform chemicals have been identified as a highly promising approach to alleviate anthropogenic CO<sub>2</sub>, providing a waste-value approach to upgrade CO<sub>2</sub> into building block and value-added products for chemical industry.<sup>1–3</sup> Due to the highly oxidized state, thermodynamic stability, and unreactive nature of CO<sub>2</sub>, economical, active, and selective catalysts are mandatory and the chemical conversion and the economical utilization of CO<sub>2</sub> are notable scientific and technical challenges.<sup>1</sup>

Numerous experimental and computational studies have shown that CO<sub>2</sub> reduction takes place at the metal–oxide interface,<sup>4–10</sup> which is also an active domain for many other industrially important catalytic reactions,<sup>11</sup> such as the water–gas shift reaction<sup>12,13</sup> and CO oxidation<sup>14,15</sup> just to mention but a few. These reactions have been reported to take place over a variety of metal–oxide interfaces with diverse chemical nature and composition, e.g., Au–TiO<sub>2</sub>,<sup>15–17</sup> Cu–ZnO,<sup>4,9</sup> Rh–ZrO<sub>2</sub>,<sup>13,18</sup> FeO–Pt,<sup>19</sup> Pd–Co<sub>3</sub>O<sub>4</sub>,<sup>20,21</sup> Pt–SiO<sub>2</sub>,<sup>22,23</sup> and others.<sup>24</sup> As the experimental characterization of interface structures at the atomic level is demanding, density functional theory (DFT) modeling is extensively used to obtain

microscopic information about chemical and structural properties of interfaces<sup>4,13,15,17,25,26</sup> and to establish structure–performance relationships.<sup>25</sup> While the catalyst models used in DFT calculations must be firmly based on real catalytic systems, simplifications are mandatory to reduce the computational burden. The key feature of a catalyst to be captured by the model is an active site. Typically, the employed models vary depending on the chemical composition and nature of the active site. For metal-only active sites, periodic surface slab models are commonly used,<sup>27–30</sup> whereas active sites consisting of the metal–oxide interface are often represented by oxide-supported metal clusters<sup>8,31–34</sup> or infinitely long nanorods.<sup>13,15,25,26</sup>

Among the possible chemical transformations, CO<sub>2</sub> conversion to methanol is particularly interesting due to the potential of methanol as a future energy carrier.<sup>2,35</sup> While Cu/ZnO/Al<sub>2</sub>O<sub>3</sub> catalysts are commonly used in industry to produce methanol from CO and they have also successfully been applied to CO<sub>2</sub> reduction to methanol,<sup>2,5,36,37</sup> ZrO<sub>2</sub> supported or promoted Cu catalysts have been identified as promising alternatives due to their higher selectivities and turn over frequencies toward methanol.<sup>5,6,38–40</sup> Recent studies indicate that a reaction mechanism and selectivity are determined by the adsorption energies of key reaction intermediates.<sup>5,8,26,31</sup> Two central reaction steps, namely, H<sub>2</sub> dissociation<sup>41,42</sup> and CO<sub>2</sub>

activation, are strongly associated with the Cu–ZrO<sub>2</sub> interface.<sup>5,38,43</sup> The reaction is inferred to be structure sensitive to Cu, and the synergy between Cu and support oxides is responsible for enhanced reactivity.<sup>4,5,44–48</sup> In calculations, however, adsorption characteristics may sensitively depend on a constructed catalyst model, and small differences between relatively similar active sites may introduce large variations in adsorption energies as shown, e.g., for CO adsorption on zirconia supported metal clusters.<sup>33</sup> Computationally, CO<sub>2</sub> conversion to methanol has recently been studied employing a Cu<sub>38</sub> cluster model supported on a *m*-ZrO<sub>2</sub>( $\bar{1}11$ ) surface<sup>8</sup> and a Cu nanorod model, which is composed of three layers of stacked Cu(100) facets on *t*-ZrO<sub>2</sub>(101).<sup>26</sup> A similar nanorod model was also used for a Au–MgO interface to address a water–gas shift reaction.<sup>12</sup> In another computational study, the catalytic properties of various metal–MgO interfaces were considered using rods that also consist of (100) terminated slices but cut in a different orientation to better match the symmetry of MgO(100).<sup>25</sup> CO<sub>2</sub> reduction on SiO<sub>2</sub> and TiO<sub>2</sub> supported Pt was, in turn, investigated using a Pt<sub>25</sub> cluster, also composed of stacked (100) facets and exposing (111) microfacets toward the interface.<sup>31</sup> A differently shaped Rh nanorod, terminated by (111) facets on each side, was employed for a water–gas shift reaction on ZrO<sub>2</sub>,<sup>13</sup> and a similar model was used for Au–TiO<sub>2</sub> to address CO oxidation<sup>15</sup> and low temperature H<sub>2</sub> oxidation.<sup>49</sup> As one would expect, the symmetry and periodicity of the underlying support oxide naturally influence the interface and must therefore be considered. For highly symmetric oxide surfaces, such as MgO(100), the orientation of a deposited nanorod has a vanishingly small impact on the interface. For less symmetric oxides, the position and orientation of the nanorod can substantially change the interface structure. For example, a monoclinic ZrO<sub>2</sub>( $\bar{1}11$ ) surface displays a less symmetric crystal structure than a tetragonal ZrO<sub>2</sub>(101) surface. One more feature that may affect interface reactivity is strain effects,<sup>25</sup> which together with defects in catalytic metal particles have been suggested to have a significant impact on catalytic efficiency.<sup>25,50,51</sup> This is hardly surprising as it is well established from the numerous studies that straining of metal surfaces changes their reactivity observed as shifts in *d*-band centers.<sup>30,52</sup> Artificial strain effects may emerge in the construction of atomic models for metal–oxide interfaces because the lattice mismatch between the metal and oxide will introduce strain along the nanorod as it has to meet the periodicity set for the support surface.

In this study, we focus on CO<sub>2</sub> adsorption and activation on various Cu–ZrO<sub>2</sub> interface structures to shed light on the influence of the interface properties on CO<sub>2</sub> binding. Specifically, we considered two Cu nanorod models with different geometries and both tetragonal [*t*-ZrO<sub>2</sub>(101)] and monoclinic [*m*-ZrO<sub>2</sub>( $\bar{1}11$ )] zirconia surfaces. A comprehensive screening of nanorod positions was performed on oxide, and CO<sub>2</sub> characteristics were analyzed for differently strained interfaces. The adsorption process was broken down to distinct electronic contributions, and they were used to attempt to establish general trends between the interface structure and its ability to adsorb and activate CO<sub>2</sub>.

## II. COMPUTATIONAL METHODS

All density functional theory (DFT) calculations were carried out using the Bayesian error estimation functional with van der

Waals correlation (BEEF-vdW)<sup>53</sup> in the projector-augmented wave (PAW)<sup>54</sup> formalism as implemented in the GPAW<sup>55</sup> package. The core electrons of all elements were described by PAW setups in the frozen-core approximation. A maximum spacing of 0.18 Å was used for the real-space grid basis, and the reciprocal space was sampled at the  $\Gamma$  point. Periodic boundary conditions were used in two directions. A Hubbard *U* correction<sup>56</sup> of 2.0 eV was applied to the *d*-orbitals of the zirconium atoms. The geometry optimizations were performed using the BFGS algorithm as implemented in the Atomic Simulation Environment (ASE).<sup>57</sup> The computed electronic structures were analyzed by the Bader partitioning method<sup>58</sup> using the code written by Tang *et al.*<sup>59</sup> to obtain the distribution of partial charges on individual atoms. The search for transition states was carried out using the climbing image nudged elastic band (NEB)<sup>60,61</sup> method. The density of states (see Figs. S7 and S8, for example) was analyzed to locate the *d*-band centers for the purpose of investigating their importance to the reactivity of the Cu nanorods according to the *d*-band model.<sup>62</sup>

The interface models were built by placing a Cu nanorod over the most stable facets of monoclinic and tetragonal zirconia surfaces, *m*-ZrO<sub>2</sub>( $\bar{1}11$ ) and *t*-ZrO<sub>2</sub>(101), as supports (see Fig. 1 for an overview). We adopted two Cu nanorod models, similar to those that have been used in previous publications,<sup>13,25,26</sup> to be used in the present study. Both models have an equal number of atoms, and they display a (111) facet toward the reactive Cu–zirconia interface. The nanorod structures differ by the facet via which they are attached to the zirconia support. The bottom interface is either a (100) facet or a (111) facet; hence, we will here call them the (100) and (111) models, respectively. As shown in Fig. 1 and Fig. S1, the (100) model has a more gently sloping reactive interface than the (111) model. Under the reaction conditions of CO<sub>2</sub> conversion to methanol, the most commonly exposed Cu surfaces are (111) and (100) of which (111) is slightly more stable.<sup>63</sup>

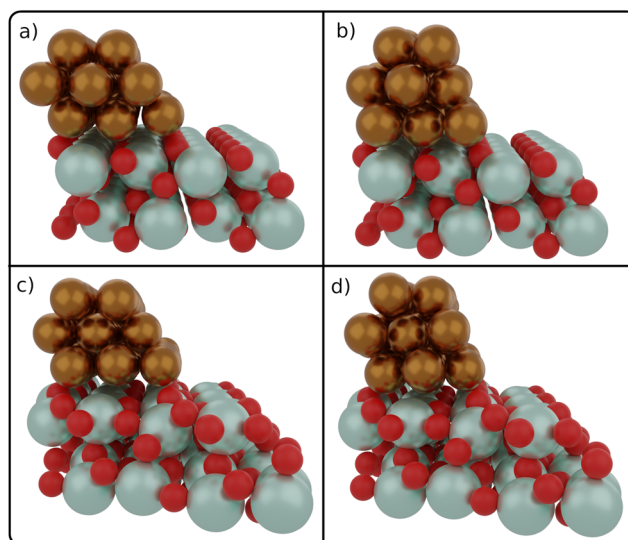


**FIG. 1.** The optimized minimum energy structures of a Cu nanorod on tetragonal or monoclinic zirconia supports. (a) (100)/*t*-ZrO<sub>2</sub>, (b) (111)/*t*-ZrO<sub>2</sub>, (c) (100)/*m*-ZrO<sub>2</sub>, and (d) (111)/*m*-ZrO<sub>2</sub>.

### A. Model system screening

Figure 1 illustrates the catalytic model systems for both nanorod models and supports. Screening of the rod position was carried out by displacing the nanorods in two directions on the support: along and perpendicular to the nanorod, while keeping the orientation fixed. To scan the surface, we used a grid of 0.7 Å steps along the nanorod axis and 1.1 or 1.5 Å steps perpendicular to the nanorod for *t*-ZrO<sub>2</sub> or *m*-ZrO<sub>2</sub>, respectively. The CO<sub>2</sub> binding was studied by attaching the molecule to one of the bottom-row Cu atoms at the reactive interface.

The oxide support was described by a slab model, the thickness of which was set to two stoichiometric layers. This approximation is necessary to reduce the computational burden, especially in the larger cells (see below). We consider the two-layer model sufficient to reveal general trends when comparing the nanorod models and justified since in preliminary evaluations with two to four layers, the Cu–zirconia binding energy showed only minor variation. We also determined that the *d*-band centers of the interfacial copper atoms varied insignificantly between different slab thicknesses. However, the CO<sub>2</sub> adsorption energy depends on slab thickness and test calculations showed that a thicker slab would enhance the binding. In geometry optimizations, the bottom layer of the zirconia slab was kept frozen at its initial bulk geometry, while the top zirconia layer, the Cu nanorod, and the possible CO<sub>2</sub> adsorbate were allowed to relax until the maximum residual force was reduced below 0.02 eV Å<sup>-1</sup>.

### B. Strain of the nanorod

With the present DFT model, we obtain a bulk Cu lattice constant of 3.69 Å, which leads to 2.61 Å nearest-neighbor Cu–Cu distance prior to modifications. Nanorods were created by repeating periodic Cu<sub>8</sub> minimum nanorod units having a length of one atom. Our computationally determined zirconia lattice constants can be found in Table S1. To explore possible implications of the artificial strain on the metal–oxide interface, we studied five different nanorod lengths on tetragonal ZrO<sub>2</sub> and three on monoclinic ZrO<sub>2</sub> surfaces; see Table S2 and Fig. S2 for details on the computational cells.

Because the calculations have to be periodic along the length of the rod, the Cu–Cu distance modified in that direction was always adjusted accordingly to meet the periodicity of the given surface unit cell. We define the strain as positive when the nanorod is stretched and negative when it is compressed relative to the computationally optimized bulk Cu lattice constant. The nanorods illustrated in Fig. 1 are those with the lowest strains, with the *t*-ZrO<sub>2</sub> support producing a -0.72% and *m*-ZrO<sub>2</sub> a -1.02% strain. Overall, the strain varies from -7.3% to +8.1% between the different surface models investigated.

### C. Energy decomposition

The energy decomposition was set to characterize different contributions in the adsorption of CO<sub>2</sub> at the catalytic sites. First, the adsorption energy of CO<sub>2</sub> was computed from the total energies as

$$\Delta E_{\text{ads}} = E_{\text{CO}_2/\text{Cu}/\text{ZrO}_2} - E_{\text{Cu}/\text{ZrO}_2} - E_{\text{CO}_2}, \quad (1)$$

where  $E_{\text{CO}_2/\text{Cu}/\text{ZrO}_2}$  stands for the full system,  $E_{\text{Cu}/\text{ZrO}_2}$  stands for the bare ZrO<sub>2</sub>-supported Cu nanorod, and  $E_{\text{CO}_2}$  stands for gas-phase (linear, inactivated) CO<sub>2</sub>. The gas-phase reference was computed in a large non-periodic cell. We will use the adsorption energy difference  $\Delta\Delta E_{\text{ads}}$  to compare the different interface model systems. Then, to exclude the contribution of atomic relaxations from the above CO<sub>2</sub>–Cu/ZrO<sub>2</sub> bond strength, we computed the total electronic interaction energy as

$$\Delta E_{\text{el}}^{\text{tot}} = E_{\text{CO}_2/\text{Cu}/\text{ZrO}_2} - E_{\text{Cu}/\text{ZrO}_2}^* - E_{\text{CO}_2}^*. \quad (2)$$

Here, asterisks stand for reference configurations, where all the atomic positions were fixed to those optimized for the full system. The adsorption and electronic interaction energies in Eqs. (1) and (2) thus differ by an energy penalty required by the deformation of the catalyst and the CO<sub>2</sub> molecule upon adsorption. Again, for comparison, we define  $\Delta\Delta E_{\text{el}}^{\text{tot}}$  to assess the difference between the models.

The electronic interaction energies between the CO<sub>2</sub> molecule and the catalyst components Cu and ZrO<sub>2</sub> were separated according to

$$\Delta E_{\text{el}}^{\text{Cu}} = E_{\text{CO}_2/\text{Cu}}^* - E_{\text{Cu}}^* - E_{\text{CO}_2}^*, \quad (3)$$

$$\Delta E_{\text{el}}^{\text{Zr}} = E_{\text{CO}_2/\text{ZrO}_2}^* - E_{\text{ZrO}_2}^* - E_{\text{CO}_2}^*. \quad (4)$$

Again, the atomic coordinates of CO<sub>2</sub> and the isolated Cu nanorod and ZrO<sub>2</sub> were fixed to those optimized for the full system. Summing Eqs. (3) and (4) together accounts for the pairwise contributions to the three-body interaction in Eq. (2). Finally, to account for the missing contribution to the total electronic interaction, we define an excess energy

$$\Delta E_{\text{exc}} = \Delta E_{\text{el}}^{\text{tot}} - \Delta E_{\text{el}}^{\text{Cu}} - \Delta E_{\text{el}}^{\text{Zr}}, \quad (5)$$

which describes the change in electronic interaction energy due to the synergy effect of the metal–oxide interface.

## III. RESULTS AND DISCUSSION

### A. Binding of the minimum-strain Cu nanorods on ZrO<sub>2</sub> supports

To evaluate how the structure and position of a nanorod on a zirconia support influence the catalytic properties of the formed interface, we carefully analyzed the binding of the two nanorods by screening their positions on zirconia. The heat maps given in Fig. 2 show how the binding energy of a nanorod depends on its position on the surface. Specifically, we plot the relative energies of both (100) and (111) models with respect to their most stable structures on both tetragonal [Figs. 2(a) and 2(b)] and monoclinic [Figs. 2(c) and 2(d)] supports. We find that the variation of the nanorod position along its length has only a minor influence on the binding energy, whereas moving the nanorod in the perpendicular direction across the zirconia surface introduces substantial energy changes. On *t*-ZrO<sub>2</sub>, the energy difference between the most stable and the least stable nanorod position is 1.4 eV for the (100) model and 2.0 eV for the (111) model. On *m*-ZrO<sub>2</sub>, the corresponding value is 2.2 eV for both models.

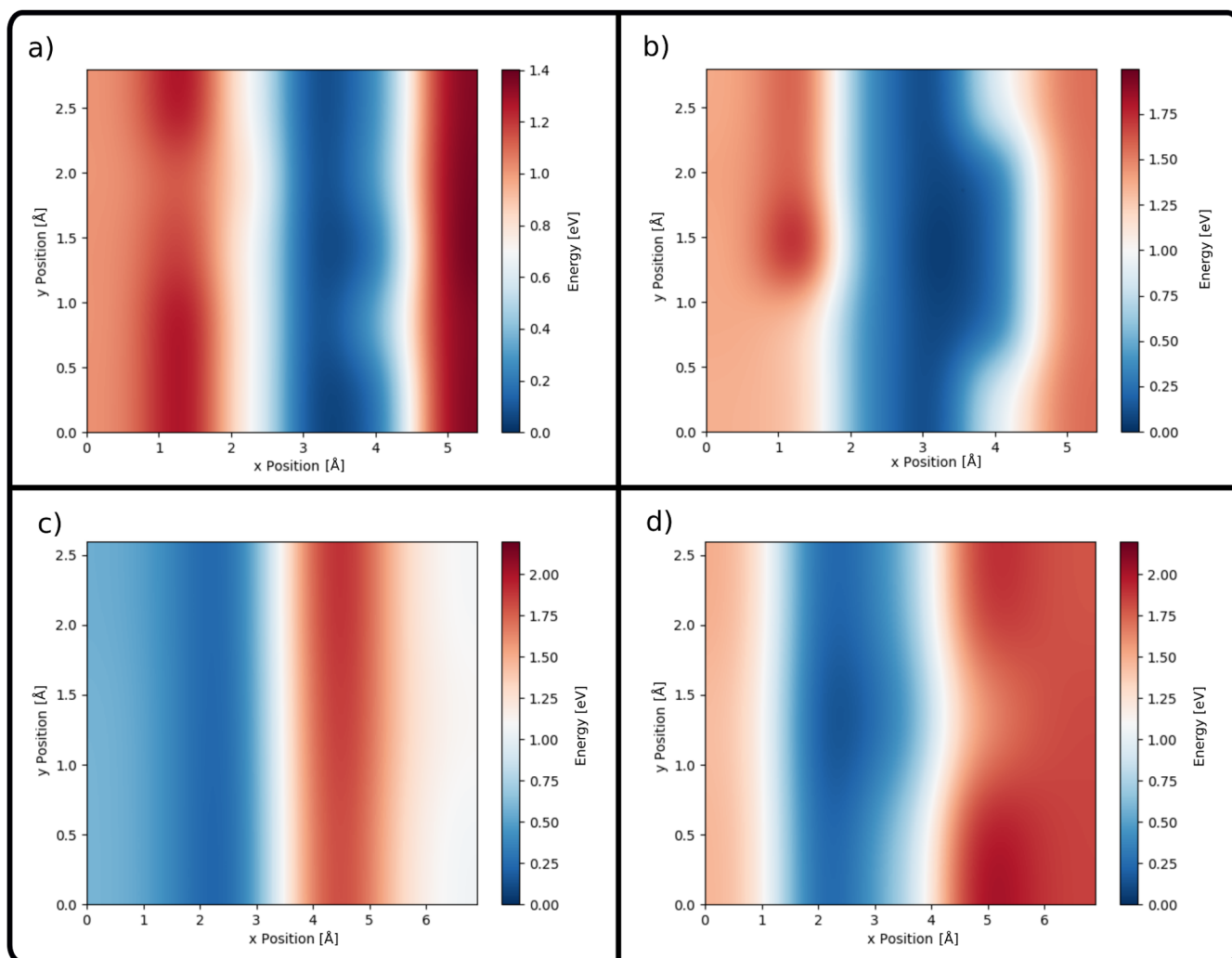


**FIG. 2.** Variation of the binding energy of a Cu nanorod across the studied zirconia surfaces: (a) (100)/*t*-ZrO<sub>2</sub>, (b) (111)/*t*-ZrO<sub>2</sub>, (c) (100)/*m*-ZrO<sub>2</sub>, and (d) (111)/*m*-ZrO<sub>2</sub>. The nanorods are oriented along the *y* axis (vertical). The position range along the *x* axis covers the surface cell length, whereas the *y*-range is limited to the nearest-neighbor Cu–Cu distance along the rod length.

We ascribe the large positional effect on the energy to the strong interaction between the bottom Cu atoms and the surface O anions. Figure 1 and Fig. S3 display the most energetically favorable interface structures for the (100) and (111) models on both tetragonal zirconia and monoclinic zirconia. Careful visual inspection of several interface structures indicates that the edge Cu atoms are attracted to surface oxygens and they avoid the positions directly above the Zr atoms. The interaction leads to the charge transfer of  $\approx 0.4$ – $0.5$  electrons from the rod to zirconia according to the Bader charge analysis. We anticipate that the positional effect, manifested in energy corrugation, would decrease with increasing nanorod width. The heat maps in Fig. 2 show that the favorable binding zone for Cu nanorods on zirconia is very narrow. Thus, wider nanorods would always spread out over unfavorable areas of zirconia as well,

which weakens the overall binding to the underlying support. The fact that the relative energy increases steeply in heat maps when Cu atoms move to Zr top sites may also have implications for binding characteristics of larger Cu nanoparticles on zirconia. Interface structures where the Cu edge atoms reside on Zr top sites should statistically appear less often as they are energetically costly, and thus, nanoparticles would prefer to create interfaces similar to those shown in Fig. 1 and Fig. S3. (For a top view of the binding interface, see Fig. S4.)

A more detailed comparison of energies of the two models shows that the (111) model is more stable than the (100) model. On *t*-ZrO<sub>2</sub>, the relative stability of the models differs by 0.11 eV/nanorod unit, while on *m*-ZrO<sub>2</sub>, the difference is as large as 0.32 eV. In the gas-phase, the (111) model is 0.33 eV/nanorod

unit more stable than the (100) model. However, as this energy difference decreases on the tetragonal zirconia surface, it implies that the interaction with the support, particularly, stabilizes the (100) Cu nanorod. We link the surface-specific stabilization effect to the Cu–O distances, which are shorter on tetragonal zirconia than on monoclinic zirconia; see Figs. S5(a) and S6. The relative stabilities of (100) and (111) nanorods on zirconia surfaces are 0.37 and 0.24 eV/nanorod unit, respectively, and they further demonstrate the ability of the tetragonal surface to better stabilize Cu than the monoclinic surface. Even when considering the adsorption of a single Cu atom, we see that adsorption is about 0.3 eV more exothermic on tetragonal zirconia. These are in line with a previous experimental study,<sup>39</sup> which reports stronger Cu–ZrO<sub>2</sub> interactions on tetragonal zirconia than on monoclinic. The comparison between the adsorption energies of Cu rods normalized to the surface area and the surface energies of relevant Cu and ZrO<sub>2</sub> surfaces shows that on monoclinic zirconia, the normalized adsorption energies are roughly half of the surface energy of *m*-ZrO<sub>2</sub>( $\bar{1}01$ ) and ca. one third of the surface energies of Cu surfaces; see Table S6. To gain more detailed understanding of the energy variation seen in the heat map plots and to link the binding energy to the microscopic structure, we plotted the energy change with respect to the most stable (111)-ZrO<sub>2</sub> structure vs the average minimum Cu–O distance between the bottom Cu atoms and topmost surface anions for different nanorod positions over both surfaces. Figures S5(a) and S6 clearly display that the (111) model is more stable than the (100) model, and for both nanorod models, the shorter distance corresponds to the more stable structure. Furthermore, the average distance of the entire Cu nanorod (bottom) from zirconia is 2.5 Å on *t*-ZrO<sub>2</sub> and 3.1 Å on *m*-ZrO<sub>2</sub>. The shorter average C–O distances and shorter nanorod–oxide distance can be explained with more exposed and symmetrically located lattice oxygens on the tetragonal surface. The optimization of bottom Cu atom positions with respect to surface oxygens is more

challenging on the monoclinic surface owing to the larger asymmetry of the surface and the fact that the surface anions are located deeper in the topmost surface layer. Additionally, we note that structural deformations in Cu nanorods originating from the interaction with the zirconia support show no correlation with the relative energy of the system, as can be seen in Fig. S5(b).

## B. Strain effects on nanorod binding

A less optimal oxide surface cell size in calculations can introduce artificial strain effects on the nanorod, and these, in turn, can influence the computed adsorption characteristics. Therefore, we analyzed strain effects more closely; for computational details, see Table S2. First, the position of the differently strained nanorods was screened over both zirconia surfaces. We find that the preferred nanorod positions are almost identical to those given in Fig. 1 and Figs. S3 and S4 for the ideal interfaces, and thus, we limit our study on the most stable nanorod positions. In particular, we aim to understand changes in nanorod binding energies due to strain and elucidate the difference between the tetragonal and monoclinic ZrO<sub>2</sub> surfaces with special emphasis on the tetragonal surface.

The last column in Table I shows that the total binding energy ( $\Delta E_b$ ) is more exothermic for the (100) model and the tetragonal surface than for the (111) model and the monoclinic surface, but it follows no obvious trend. To understand the origin of this variation better, the thermodynamic cycle (see Fig. 3) was devised to analyze the different components. The cycle divides the Cu–ZrO<sub>2</sub> binding energy into four contributions. The first three steps constitute the changes in the gas-phase nanorod, and the last one measures the pure electronic interaction with zirconia. Step 1 describes the change for the optimization of interatomic Cu–Cu distances, whereas step 2 gives the energy change originating from strain

**TABLE I.** Nanorod binding energies (in eV) at each stage of the thermodynamic cycle shown in Fig. 3.  $\Delta E_b$  stands for binding energy of a nanorod to the zirconia surface and step 5 in the thermodynamic cycle. To facilitate comparison, the energies are divided by the number of rod units in the corresponding cell.

ZrO <sub>2</sub>	Nanorod	Strain (%)	Step 1	Step 2	Step 3	Step 4	$\Delta E_b$
<i>t</i> -ZrO <sub>2</sub>	(100)	-7.34	-0.034	+0.159	-0.363	-1.069	-1.306
		-2.71	-0.034	+0.002	-0.005	-1.025	-1.061
		-0.72	-0.034	+0.021	+0.007	-1.108	-1.113
		+4.24	-0.034	+0.220	+0.014	-1.183	-0.983
		+8.10	-0.034	+0.456	+0.055	-1.256	-0.779
<i>t</i> -ZrO <sub>2</sub>	(111)	-7.34	-0.012	+0.205	-0.199	-0.871	-0.877
		-2.71	-0.012	+0.003	+0.035	-0.994	-0.968
		-0.72	-0.012	+0.008	+0.102	-1.010	-0.912
		+4.24	-0.012	+0.168	+0.045	-1.039	-0.838
		+8.10	-0.012	+0.390	+0.120	-1.136	-0.638
<i>m</i> -ZrO <sub>2</sub>	(100)	-1.02	-0.019	+0.008	+0.067	-0.787	-0.741
	(111)	-4.02	-0.012	+0.035	+0.002	-0.714	-0.579
		-1.02	-0.012	+0.001	+0.009	-0.743	-0.673
		+5.57	-0.012	+0.225	+0.072	-0.898	-0.667

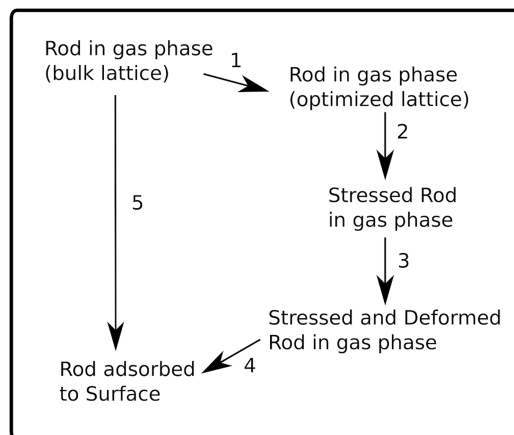


FIG. 3. A thermodynamic cycle for the binding energy decomposition of a Cu nanorod on  $ZrO_2$ .

effects, and step 3 represents the energy change due to structure deformation arising from the interaction between the nanorod and zirconia. The remaining contribution, step 4, defines the pure electronic binding interaction between the deformed Cu nanorod and zirconia.

The energy changes accompanying the thermodynamic steps are collected in Table I. Overall, the contributions from steps 1–3 are small compared to step 4, which dominates. The slight energy decrease seen in step 1 for all the models indicates that the Cu bulk lattice constant is not optimal for the gas-phase nanorod. In fact, the Cu–Cu distance decreases from the bulk value of 2.61 Å to 2.58 Å for both nanorod models on  $m$ - $ZrO_2$  and to 2.55 (2.57) Å for the (100) model [(111) model] on  $t$ - $ZrO_2$ . Other minor variations in Cu–Cu distances and energies in step 1 originate from the differences in the computational cell shapes. As expected, increasing strain leads to a positive (endothermic) energy change in step 2 as mainly also does nanorod deformation in step 3. While irregularities introduced by the support make it difficult to predict clear trends, the larger strain is accompanied by stronger deformation and this is especially clear for the two most strained (100) rods.

Cu nanorod binding energy on zirconia is dominated by electronic interaction (step 4), which is more exothermic for  $t$ - $ZrO_2$  than for  $m$ - $ZrO_2$  resulting most likely from the shorter Cu–O distance as also suggested for the minimum-strain interfaces. As illustrated in Fig. S9, the introduced strain correlates well with the electronic interaction energy, where the compression of the nanorod decreases the electronic interaction between Cu and zirconia, while the expansion of the nanorod enhances it. No clear correlation is seen when attempting to link binding energies to strain. Multiple factors may contribute to this, the main reason being the irregular structural deformations during structure optimization. The  $d$ -band-center analysis supports the stronger interaction between Cu and tetragonal zirconia as the shifts in the  $d$ -band center are larger for tetragonal than for monoclinic surfaces. The net shift, see Table S3, is to lower energies, and it is dominated by the “ligand” effect introduced by the oxide, whereas the “strain” effect, including deformation, constitutes minor contribution.

### C. $CO_2$ adsorption and activation

In order to estimate the significance of an interface site to  $CO_2$  adsorption and activation, we conducted a thorough screening of the available sites for the structures explored in Sec. III A. In agreement with previous calculations,<sup>8,26</sup> we find that  $CO_2$  adsorbs preferably in a bent configuration for the minimum-strain interface structures, as shown in Figs. 4 and 5. Our results also demonstrate that adsorption energies depend sensitively on the nanorod model and the interface structure.

Figure 4 displays the minimum-strain Cu– $t$ - $ZrO_2$  interface for which the most exothermic  $CO_2$  adsorption energies were computed to be  $-1.01$  and  $-0.52$  eV for the (100) and (111) models, respectively.  $CO_2$  adsorption to Cu– $m$ - $ZrO_2$  is an activated process to Cu– $m$ - $ZrO_2$ ( $\bar{1}11$ ) with the activation energy of 0.38 eV with respect to physisorbed  $CO_2$  computed with the NEB. The adsorption energies for other interfacial sites along these interfaces can be found in Table S4. A previous DFT study<sup>26</sup> reports as large as  $-1.78$  eV adsorption energy for  $CO_2$  with the (100) model. We associate the large difference with two factors: first, a  $+0.41$  eV gas-phase correction was applied to  $CO_2$ <sup>26</sup> and second, to the fact that the employed interface model has substantial, 5.08%, strain, which strongly impacts  $CO_2$  adsorption, as discussed below. Figure 5 illustrates the  $CO_2$  adsorption on the Cu– $m$ - $ZrO_2$  interface, where the computed  $CO_2$  adsorption energies are  $-1.38$  eV for the (100) nanorod and  $-0.44$  eV for the (111) nanorod. For a  $Cu_{38}$ - $m$ - $ZrO_2$ ( $\bar{1}11$ ) interface, the  $CO_2$  adsorption energy is  $-1.86$  eV<sup>8</sup> being substantially more exothermic than what we found in this work. This time, the observed adsorption energy difference is attributed, on one hand, to the different exchange and correlation functional and, on the other hand, to the 38-atom cluster geometry. In another computational work, an adsorption energy of  $-0.69$  eV was reported for a slightly thinner (111)-type Cu nanorod on a stepped  $m$ - $ZrO_2$ ( $\bar{2}12$ ) surface,<sup>7</sup> where  $CO_2$  is at the interface but binds only to the Cu atoms.

The most stable  $CO_2$  adsorption geometries are structurally similar for both zirconia surfaces and nanorod models.  $CO_2$  prefers a bidentate geometry, i.e., it binds to Cu via the carbon atom and has both oxygen atoms pointing down toward the support cations with the O–C–O angle being close to  $120^\circ$ . A substantial deviation from the linear gas-phase structure and a slight, 0.14 Å, elongation of the C–O bonds clearly indicate  $CO_2$  activation. This is further supported by the Bader charge analysis, showing that the  $CO_2$  molecule gains 1.2  $|e|$  upon adsorption to the Cu– $ZrO_2$  interfaces, as seen in Table S7, which is in line with the previously reported value.<sup>8</sup> The angle and charge of adsorbed  $CO_2$  are similar to those of gas-phase formic acid for which the calculated O–C–O angle is  $125^\circ$  and the charge of the COO skeleton is  $-1.26 |e|$ . After  $CO_2$  adsorption, the nanorod is charged positively by around 1.3  $|e|$  (see Table S7). The anionic behavior of the  $CO_2$  molecule reflects reductive activation due to the metal contacts. Interaction between  $CO_2$  and the interface introduces structural deformations to the Cu nanorods. While in the case of the  $t$ - $ZrO_2$  surface, the distortion of the Cu edge is minor, on  $m$ - $ZrO_2$ ,  $CO_2$  clearly pulls out one Cu atom from both the nanorods; see Fig. 5.

Table II summarizes the energy contributions defined in Eqs. (1)–(5) and displays the origin of the variation of  $CO_2$  adsorption energies from one minimum-strain interface to the other. We

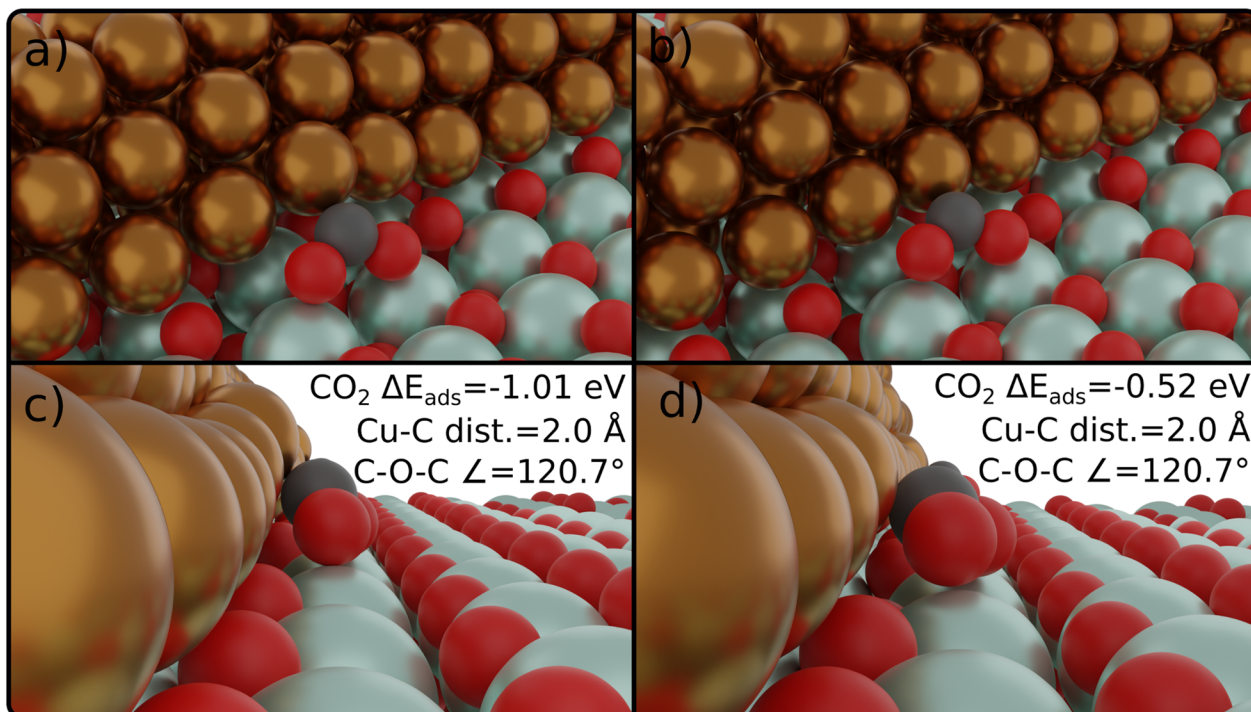


**FIG. 4.** Front and side views of the most stable CO<sub>2</sub> adsorption geometry at the minimum-strain Cu-*f*-ZrO<sub>2</sub> interfaces for the (100) model [(a) and (c)] and the (111) model [(b) and (d)].

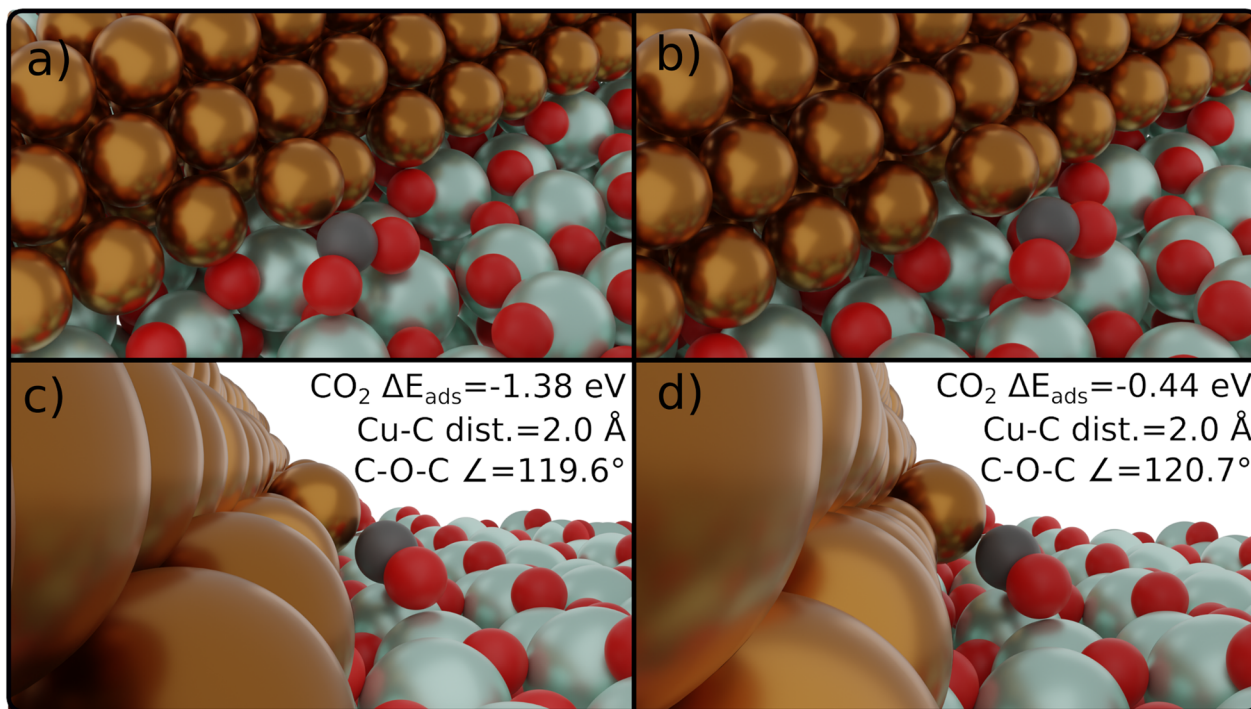


**FIG. 5.** Front and side views of the most stable CO<sub>2</sub> adsorption geometry at the minimum-strain Cu-*m*-ZrO<sub>2</sub> interfaces for the (100) model [(a) and (c)] and the (111) model [(b) and (d)].

**TABLE II.** CO<sub>2</sub> adsorption energies ( $\Delta E_{\text{ads}}$ ) and electronic interaction energies ( $\Delta E_{\text{el}}^{\text{tot}}$ ,  $\Delta E_{\text{el}}^{\text{Cu}}$ ,  $\Delta E_{\text{el}}^{\text{Zr}}$ , and  $\Delta E_{\text{exc}}$ ), defined in Eqs. (2)–(5) for different models and strain values. All the energy values are given in eV.

ZrO <sub>2</sub>	Nanorod	Strain (%)	$\Delta E_{\text{ads}}$	$\Delta E_{\text{el}}^{\text{tot}}$	$\Delta E_{\text{el}}^{\text{Cu}}$	$\Delta E_{\text{el}}^{\text{Zr}}$	$\Delta E_{\text{exc}}$
<i>t</i> -ZrO <sub>2</sub>	(100)	−0.72	−1.01	−6.30	−2.49	−1.76	−2.05
		+4.24	−1.17	−6.39	−2.86	−1.63	−1.89
	(111)	−7.34	−1.91	−6.02	−2.34	−1.55	−2.13
		−2.71	−0.51	−5.84	−2.38	−1.85	−1.60
		−0.72	−0.52	−5.55	−2.58	−1.50	−1.47
		+4.24	−0.71	−5.98	−2.49	−1.63	−1.87
<i>m</i> -ZrO <sub>2</sub>	(100)	+8.10	−1.33	−6.27	−2.17	−1.39	−2.71
		−1.02	−1.38	−6.06	−2.13	−1.63	−2.30
	(111)	−4.02	−0.89	−5.79	−1.88	−1.72	−2.18
		−1.02	−0.44	−5.57	−1.78	−1.62	−2.18
		+5.57	−1.34	−5.81	−2.69	−1.70	−1.42

first focus on electronic interaction energies, which exclude all the structural deformations. For example, the adsorption energy difference ( $\Delta\Delta E_{\text{ads}}$ ) between the (100) and (111) models is 0.49 eV for the tetragonal surface, whereas the pure electronic, aka binding, interaction energy difference,  $\Delta\Delta E_{\text{el}}^{\text{tot}}$ , shows a larger, 0.75 eV, value. Interestingly, for the monoclinic surface,  $\Delta\Delta E_{\text{ads}}$  is larger than  $\Delta\Delta E_{\text{el}}^{\text{tot}}$  (0.9 vs 0.5 eV). The opposite behavior is ascribed to non-identical atomic relaxations for different CO<sub>2</sub>-interface systems. The deformation energies vary heavily from one system to the other, where the bending of the CO<sub>2</sub> molecules is the dominant contribution. However, the differences in deformation penalties between rods of different structures are not consistent with the differences in adsorption energies. In general, we attribute the observed adsorption energy differences to different electronic interaction energies, which are clearly more exothermic for the (100) model on both tetragonal zirconia and monoclinic zirconia. The interaction energies from the CO<sub>2</sub>-Cu and CO<sub>2</sub>-ZrO<sub>2</sub> subsystems, which measure the binding between CO<sub>2</sub> and metal and CO<sub>2</sub> and oxide, do not indicate that one nanorod model or zirconia crystal structure is favored over the other. The substantial synergy between Cu and zirconia is demonstrated by the exothermic values of  $\Delta E_{\text{exc}}$  for all the studied system. This is reflected by larger charge transfer to CO<sub>2</sub> at the interface compared to the individual CO<sub>2</sub>-Cu and CO<sub>2</sub>-ZrO<sub>2</sub> subsystems, as can be seen in Table S7

Next, a CO<sub>2</sub> adsorption site at the (111)-ZrO<sub>2</sub> interface is further explored by moving the nanorod across the oxide surfaces. Figure 6 displays the heat maps summarizing the energy variation with respect to the most stable adsorption structure at the interface. The plots show that for many nanorod positions, CO<sub>2</sub> does not either adsorb at all or adsorption is energetically very unfavorable. In order to interpret the heat map information, we analyzed the calculated CO<sub>2</sub> adsorption structures. For a favorable CO<sub>2</sub> adsorption, it seems to be crucial to have lattice Zr cations sufficiently close to the Cu edge to ensure that the oxygens of the CO<sub>2</sub> molecule can interact with them. The nanorod positions, where surface anions are

closer to the Cu edge than the Zr cations, lead to unfavorable CO<sub>2</sub> adsorption due to repulsive interactions between the oxygen atoms and anions. The central role of the zirconia support is further highlighted by the fact that, without the support, CO<sub>2</sub> only physisorbs maintaining a linear structure on a Cu(111) surface and on our (111) and (100) nanorods. This agrees well with the previous DFT results, which also demonstrate CO<sub>2</sub> physisorption on Cu(111) and Cu(533) surfaces.<sup>28,37</sup>

CO<sub>2</sub> adsorption on the bare zirconia surface leads to carbonate (CO<sub>3</sub>) formation with the lattice oxygen. We find this process exothermic by −0.57 eV on *t*-ZrO<sub>2</sub> and by −0.59 eV on *m*-ZrO<sub>2</sub>. In the case of a (111) model, the carbonate formation is thermodynamically slightly more favorable than CO<sub>2</sub> adsorption at the interface, which makes these two simultaneous reactions competing. On the other hand, CO<sub>2</sub> adsorption at the interface is clearly preferred to carbonate formation for the (100) model. Previously computed<sup>64</sup> carbonate formation energy on the same monoclinic zirconia surface is about −1.13 eV, which is substantially more exothermic than the value reported here. We ascribe this energy difference to the different exchange and correlation functional and to the thicker zirconia slab, not computationally feasible for the present screening study. Note that under the reaction conditions, zirconia is partially covered by OH groups, which are known to react with CO<sub>2</sub> to create an extremely stable formate species.<sup>6,13,64,65</sup>

We close the discussion on CO<sub>2</sub> adsorption and activation by considering that at the strained metal-oxide interfaces. Similar to the minimum-strained nanorods, CO<sub>2</sub> is activated via electron transfer and the molecule adopts a bent adsorption configuration. The bidentate binding is preferred, while monodentate geometries also appear at slightly higher energies. CO<sub>2</sub> adsorption energies and the electronic interaction energy components for the strained interfaces are presented in Table II. While the data do not allow to make comprehensive conclusions for all the interfaces, we can say that for the (111) model, the straining and compressing of the nanorod lead to more exothermic electronic interaction energies. However, one has

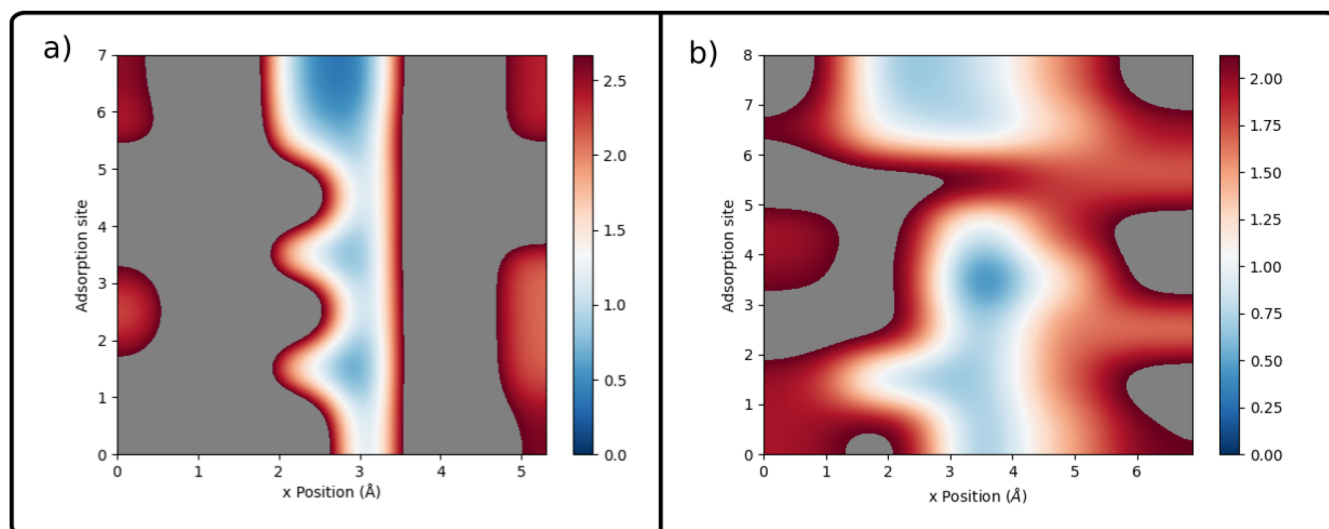


**FIG. 6.** Heat maps for CO<sub>2</sub> adsorption upon varying the position of the (111) nanorod across the (a) *t*-ZrO<sub>2</sub> and (b) *m*-ZrO<sub>2</sub> surfaces. The nanorod lies parallel to the vertical axis and is moved along the horizontal axis. The energy difference is given with respect to the most stable adsorption structure. The vertical axis numbers represent Cu edge atoms to which CO<sub>2</sub> was attempted to bind. Gray color corresponds to the nanorod positions, which do not bind or activate CO<sub>2</sub>.

to be careful with the nanorods exposed to larger ( $\pm > 7\%$ ) strain as they experienced significant structural deformations during the atomic structure optimization, which reduced the atomic coordination number of some Cu atoms, typically those interacting with the C atom leading to enhanced CO<sub>2</sub> adsorption. Therefore, these systems are largely omitted from the detailed discussion. In general, adsorption and total electronic interaction energies do not correlate. This means that adsorption energy difference and total electronic interaction energy difference,  $\Delta\Delta E_{\text{ads}}$  and  $\Delta\Delta E_{\text{el}}^{\text{tot}}$ , differ for a considered system pair. Again, this can be attributed to diverse deformations of the nanorod and the molecule, giving system-specific positive deformation energies. In addition, we see for all the systems strong synergy between the metal and oxide, which is reflected by exothermic values of  $\Delta E_{\text{exc}}$  and highlights the unique nature of the interface. Table II also shows that interfaces built from the (100) nanorod give more exothermic CO<sub>2</sub> adsorption energies than its (111) counterpart.

In order to understand the variation of CO<sub>2</sub> adsorption energy from one system to the other, we performed *d*-band-center analysis separately to each step in the thermodynamic cycle. The formation of a metal–oxide interface has been considered as a two-step process,<sup>25</sup> including the “strain” and “ligand” contributions similar to bimetallic systems.<sup>66</sup> The “strain” effects include both changes in Cu–Cu distances along the nanorod and structural deformation of the nanorod due to interaction with zirconia, whereas the ligand effect describes the electronic interactions between Cu and zirconia. The first three steps in the thermodynamic cycle contribute to the shift of the *d*-band center due to strain effects  $\Delta\epsilon_d^{\text{strain}}$ , while the shift of the *d*-band center for step 4 ( $\Delta\epsilon_d^{\text{ligand}}$ ) measures the change resulting from the ligand effect. The overall impact of the support on the Cu nanorod is a clear shift of a *d*-band center to lower energies for all the models; see Table S3 for explicit

numerical values. The ligand effects clearly dominate, and the negative value of  $\Delta\epsilon_d^{\text{ligand}}$  for all the interface models highlights that binding interaction between Cu and zirconia shifts the *d*-band center to lower energies. The contribution of the strain effects to the shift of the *d*-band center is negligible, being positive for some interfaces and negative for some others. Table S3 shows that CO<sub>2</sub> adsorption energies cannot be rationalized with the shift of the *d*-band center as no correlation can be established between the adsorption energy and the total shift in the *d*-band center. We believe that the complex metal–oxide interaction effects at the interface together with structural deformations, especially in the case of the less stable (100) rod, make the *d*-band model insufficient to explain CO<sub>2</sub> adsorption energies.

Altogether, our DFT results highlight that CO<sub>2</sub> adsorption and activation depend sensitively on the atomic structure and composition, making only few site geometries favorable for CO<sub>2</sub>. Moreover, care must be taken when building computational interface models as artificial strain enhances CO<sub>2</sub> adsorption, and similar effects might be present for reaction intermediates as well, let alone that the possible strain effects may affect the activation barriers for elementary steps taking place at the interface. Structure sensitivity of CO<sub>2</sub> adsorption suggests that not all the Cu–ZrO<sub>2</sub> interfaces at real-world catalytic systems are active toward CO<sub>2</sub> chemistry. This is because supported nanoparticles present various interface sites with different compositions and atomic structures, and their direct structural optimization is infeasible.

#### IV. CONCLUSIONS

We have investigated the properties of a Cu–ZrO<sub>2</sub> interface and its ability to adsorb and activate CO<sub>2</sub> using density functional theory calculations. Specifically, two Cu nanorod models were explored on *m*-ZrO<sub>2</sub>( $\bar{1}11$ ) and *t*-ZrO<sub>2</sub>(101) surfaces. We observed that the (111)

nanorod model is always more stable than the (100) one regardless of whether it is supported by zirconia or not. Tetragonal  $\text{ZrO}_2$  stabilizes both nanorod models more than monoclinic  $\text{ZrO}_2$ , which is likely due to the more exposed oxygen anions of the  $t\text{-ZrO}_2(101)$  surface. Our calculations demonstrate that the stability of the nanorod depends sensitively on its local chemical environment on  $\text{ZrO}_2$  and results from the fact that Cu atoms avoid the interaction with surface cations and prefer to minimize a Cu-anion nearest-neighbor distance. Compression along the nanorod enhances binding to zirconia, while tension of the nanorod weakens the interaction with the studied oxide surfaces.

Our results demonstrate that the employed Cu– $\text{ZrO}_2$  interface model significantly impacts the adsorption characteristics of the  $\text{CO}_2$  molecule. In general, the interfaces built using the (100) nanorod adsorb  $\text{CO}_2$  more strongly compared to the interfaces created with the (111) nanorods. The activation of  $\text{CO}_2$  is seen as clearly negative Bader charge originating from the synergy between Cu and  $\text{ZrO}_2$  and a bent adsorption configuration. Applying strain to the nanorod enhances electronic interaction with  $\text{CO}_2$ , which is not always reflected in more exothermic adsorption energies due to structural deformation effects. The excess interaction energy originating from the synergy between the metal and the support is strongly exothermic for the all studied systems, highlighting the importance of the metal–oxide interface. Furthermore, depending on how the nanorod is positioned on  $\text{ZrO}_2$ ,  $\text{CO}_2$  might not adsorb at the interface at all.

Overall, not only the chemical composition but also the diverse structural features of an interface can impact the adsorption characteristics of reacting molecules and, consequently, the computed activity and selectivity profiles. Therefore, when building computational models for catalytic reactions taking place at the metal–oxide interface, care should be taken in constructing interfaces and identifying interfacial active sites.

## SUPPLEMENTARY MATERIAL

See the [supplementary material](#) for details on the construction and the structure of the atomic models, density of states plots, and the  $d$ -band shifts for the thermodynamic cycle.

## ACKNOWLEDGMENTS

This work was funded by the Academy of Finland under Project Nos. 329977 and 307623 and the University of Jyväskylä. The electronic structure calculations were made possible by the computational resources provided by the CSC—IT Center for Science, Espoo, Finland (<https://www.csc.fi/en/>), and the Finnish Grid and Cloud Infrastructure.

## DATA AVAILABILITY

The data that support the findings of this study are available from the corresponding author upon reasonable request.

## REFERENCES

- S. Roy, A. Cherevotan, and S. C. Peter, *ACS Energy Lett.* **3**, 1938 (2018).
- B. M. Tackett, E. Gomez, and J. G. Chen, *Nat. Catal.* **2**, 381 (2019).
- R. P. Ye, J. Ding, W. Gong, M. D. Argyle, Q. Zhong, Y. Wang, C. K. Russell, Z. Xu, A. G. Russell, Q. Li, M. Fan, and Y. G. Yao, *Nat. Commun.* **10**, 5698 (2019).
- S. Kattel, P. J. Ramirez, J. G. Chen, J. A. Rodriguez, and P. Liu, *Science* **355**, 1296 (2017).
- S. Kattel, P. Liu, and J. G. Chen, *J. Am. Chem. Soc.* **139**, 9739 (2017).
- N. Scotti, F. Bossola, F. Zaccheria, and N. Ravasio, *Catalysts* **10**, 168 (2020).
- Q.-L. Tang, Q.-J. Hong, and Z.-P. Liu, *J. Catal.* **263**, 114 (2009).
- K. Larmier, W.-C. Liao, S. Tada, E. Lam, R. Verel, A. Bansode, A. Urakawa, A. Comas-Vives, and C. Copéret, *Angew. Chem., Int. Ed.* **56**, 2318 (2017).
- M. Zabilskiy, V. L. Sushkevich, D. Palagin, M. A. Newton, F. Krumeich, and J. A. van Bokhoven, *Nat. Commun.* **11**, 2409 (2020).
- Y. Wang, S. Kattel, W. Gao, K. Li, P. Liu, J. G. Chen, and H. Wang, *Nat. Commun.* **10**, 1166 (2019).
- Q. Fu and T. Wagner, *Surf. Sci. Rep.* **62**, 431 (2007).
- Z.-J. Zhao, Z. Li, Y. Cui, H. Zhu, W. F. Schneider, W. N. Delgass, F. Ribeiro, and J. Greeley, *J. Catal.* **345**, 157 (2017).
- M. M. Kauppinen, M. M. Melander, A. S. Bazhenov, and K. Honkala, *ACS Catal.* **8**, 11633 (2018).
- Y. Y. Wu, N. A. Mashayekhi, and H. H. Kung, *Catal. Sci. Technol.* **3**, 2881 (2013).
- I. X. Green, W. Tang, M. Neurock, and J. T. Yates, *Science* **333**, 736 (2011).
- M. Boronat and A. Corma, *Dalton Trans.* **39**, 8538 (2010).
- P. Schlexer, D. Widmann, R. J. Behm, and G. Pacchioni, *ACS Catal.* **8**, 6513 (2018).
- H. Tao, C. Choi, L.-X. Ding, Z. Jiang, Z. Han, M. Jia, Q. Fan, Y. Gao, H. Wang, A. W. Robertson, S. Hong, Y. Jung, S. Liu, and Z. Sun, *Chem* **5**, 204 (2019).
- Q. Fu, W.-X. Li, Y. Yao, H. Liu, H.-Y. Su, D. Ma, X.-K. Gu, L. Chen, Z. Wang, H. Zhang, B. Wang, and X. Bao, *Science* **328**, 1141 (2010).
- J.-Y. Luo, M. Meng, X. Li, X.-G. Li, Y.-Q. Zha, T.-D. Hu, Y.-N. Xie, and J. Zhang, *J. Catal.* **254**, 310 (2008).
- J. Shen, R. E. Hayes, and N. Semagina, *Catal. Today* **360**, 435 (2021).
- N. T. S. Phan, M. Van Der Sluys, and C. W. Jones, *Adv. Synth. Catal.* **348**, 609 (2006).
- V. Polshettiwar, C. Len, and A. Fihri, *Coord. Chem. Rev.* **253**, 2599 (2009).
- Z.-c. Zhang, B. Xu, and X. Wang, *Chem. Soc. Rev.* **43**, 7870 (2014).
- P. Mehta, J. Greeley, W. N. Delgass, and W. F. Schneider, *ACS Catal.* **7**, 4707 (2017).
- S. Polierer, J. Jelic, S. Pitter, and F. Studt, *J. Phys. Chem. C* **123**, 26904 (2019).
- J. K. Nørskov, T. Bligaard, J. Rossmeisl, and C. H. Christensen, *Nat. Chem.* **1**, 37 (2009).
- D. Kopač, B. Likozar, and M. Huš, *Appl. Surf. Sci.* **497**, 143783 (2019).
- I. A. Pašti and S. V. Mentus, *Electrochim. Acta* **55**, 1995 (2010).
- M. Mavrikakis, B. Hammer, and J. K. Nørskov, *Phys. Rev. Lett.* **81**, 2819 (1998).
- S. Kattel, B. Yan, J. G. Chen, and P. Liu, *J. Catal.* **343**, 115 (2016).
- M. M. Kauppinen, V. Korpelin, A. M. Verma, M. M. Melander, and K. Honkala, *J. Chem. Phys.* **151**, 164302 (2019).
- A. S. Bazhenov and K. Honkala, *J. Phys. Chem. C* **123**, 7209 (2019).
- Y. Yang, J. Evans, J. A. Rodriguez, M. G. White, and P. Liu, *Phys. Chem. Chem. Phys.* **12**, 9909 (2010).
- G. A. Olah, *Angew. Chem., Int. Ed.* **52**, 104 (2013).
- M. Behrens, F. Studt, I. Kasatkin, S. Kuhl, M. Havecker, F. Abild-Pedersen, S. Zander, F. Girgsdies, P. Kurr, B.-L. Kniep, M. Tovar, R. W. Fischer, J. K. Nørskov, and R. Schlögl, *Science* **336**, 893 (2012).
- L. C. Grabow and M. Mavrikakis, *ACS Catal.* **1**, 365 (2011).
- S. Kattel, B. Yan, Y. Yang, J. G. Chen, and P. Liu, *J. Am. Chem. Soc.* **138**, 12440 (2016).
- T. Witoon, J. Chalorngtham, P. Dumrongbunditkul, M. Chareonpanich, and J. Limtrakul, *Chem. Eng. J.* **293**, 327 (2016).
- Y. Nitta, O. Suwata, Y. Ikeda, Y. Okamoto, and T. Imanaka, *Catal. Lett.* **26**, 345 (1994).
- K.-D. Jung and A. T. Bell, *J. Catal.* **193**, 207 (2000).
- I. A. Fisher and A. T. Bell, *J. Catal.* **178**, 153 (1998).
- I. A. Fisher, H. C. Woo, and A. T. Bell, *Catal. Lett.* **44**, 11 (1997).

- <sup>44</sup>F. Arena, G. Italiano, K. Barbera, S. Bordiga, G. Bonura, L. Spadaro, and F. Frusteri, *Appl. Catal., A* **350**, 16 (2008).
- <sup>45</sup>F. Arena, G. Mezzatesta, G. Zafarana, G. Trunfio, F. Frusteri, and L. Spadaro, *J. Catal.* **300**, 141 (2013).
- <sup>46</sup>J.-D. Grunwaldt, A. M. Molenbroek, N.-Y. Topsøe, H. Topsøe, and B. S. Clausen, *J. Catal.* **194**, 452 (2000).
- <sup>47</sup>A. Le Valant, C. Comminges, C. Tisseraud, C. Canaff, L. Pinard, and Y. Pouilloux, *J. Catal.* **324**, 41 (2015).
- <sup>48</sup>J. Zhong, X. Yang, Z. Wu, B. Liang, Y. Huang, and T. Zhang, *Chem. Soc. Rev.* **49**, 1385 (2020).
- <sup>49</sup>I. X. Green, W. Tang, M. Neurock, and J. T. Yates, Jr., *Angew. Chem., Int. Ed.* **50**, 10186 (2011).
- <sup>50</sup>I. Kasatkin, P. Kurr, B. Knier, A. Trunschke, and R. Schlögl, *Angew. Chem., Int. Ed.* **46**, 7324 (2007).
- <sup>51</sup>M. M. Günter, T. Ressler, B. Bems, C. Büscher, T. Genger, O. Hinrichsen, M. Muhler, and R. Schlögl, *Catal. Lett.* **71**, 37 (2001).
- <sup>52</sup>S. Sakong and A. Groß, *Surf. Sci.* **525**, 107 (2003).
- <sup>53</sup>J. Wellendorff, K. T. Lundgaard, A. Møgelhøj, V. Petzold, D. D. Landis, J. K. Nørskov, T. Bligaard, and K. W. Jacobsen, *Phys. Rev. B* **85**, 235149 (2012).
- <sup>54</sup>P. E. Blöchl, *Phys. Rev. B* **50**, 17953 (1994).
- <sup>55</sup>J. Enkovaara, C. Rostgaard, J. J. Mortensen, J. Chen, M. Dulak, L. Ferrighi, J. Gavnholt, C. Glinsvad, V. Haikola, H. A. Hansen, H. H. Kristoffersen, M. Kuisma, A. H. Larsen, L. Lehtovaara, M. Ljungberg, O. Lopez-Acevedo, P. G. Moses, J. Ojanen, T. Olsen, V. Petzold, N. A. Romero, J. Stausholm-Møller, M. Strange, G. A. Tritsarlis, M. Vanin, M. Walter, B. Hammer, H. Häkkinen, G. K. H. Madsen, R. M. Nieminen, J. K. Nørskov, M. Puska, T. T. Rantala, J. Schiøtz, K. S. Thygesen, and K. W. Jacobsen, *J. Phys.: Condens. Matter* **22**, 253202 (2010).
- <sup>56</sup>S. L. Dudarev, G. A. Botton, S. Y. Savrasov, C. J. Humphreys, and A. P. Sutton, *Phys. Rev. B* **57**, 1505 (1998).
- <sup>57</sup>A. H. Larsen, J. J. Mortensen, J. Blomqvist, I. E. Castelli, R. Christensen, M. Dulak, J. Friis, M. N. Groves, B. Hammer, C. Hargus, E. D. Hermes, P. C. Jennings, P. B. Jensen, J. Kermode, J. R. Kitchin, E. L. Kolsbjerg, J. Kubal, K. Kaasbjerg, S. Lysgaard, J. B. Maronsson, T. Maxson, T. Olsen, L. Pastewka, A. Peterson, C. Rostgaard, J. Schiøtz, O. Schütt, M. Strange, K. S. Thygesen, T. Vegge, L. Vilhelmsen, M. Walter, Z. Zeng, and K. W. Jacobsen, *J. Phys.: Condens. Matter* **29**, 273002 (2017).
- <sup>58</sup>R. F. W. Bader, in *Atoms in Molecules: A Quantum Theory*, International Series of Monographs on Chemistry, edited by R. F. W. Bader (Oxford University Press, Oxford, 1990).
- <sup>59</sup>W. Tang, E. Sanville, and G. Henkelman, *J. Phys.: Condens. Matter* **21**, 084204 (2009).
- <sup>60</sup>G. Henkelman, B. P. Uberuaga, and H. Jónsson, *J. Chem. Phys.* **113**, 9901 (2000).
- <sup>61</sup>G. Henkelman and H. Jónsson, *J. Chem. Phys.* **113**, 9978 (2000).
- <sup>62</sup>B. Hammer and J. K. Nørskov, *Surf. Sci.* **343**, 211 (1995).
- <sup>63</sup>P. L. Hansen, J. B. Wagner, S. Helveg, J. R. Rostrup-Nielsen, B. S. Clausen, and H. Topsøe, *Science* **295**, 2053 (2002).
- <sup>64</sup>S. Kouva, J. Andersin, K. Honkala, J. Lehtonen, L. Lefferts, and J. Kanervo, *Phys. Chem. Chem. Phys.* **16**, 20650 (2014).
- <sup>65</sup>A. S. Bazhenov and K. Honkala, *Top. Catal.* **60**, 382 (2017).
- <sup>66</sup>J. R. Kitchin, J. K. Nørskov, M. A. Barteau, and J. G. Chen, *Phys. Rev. Lett.* **93**, 156801 (2004).